

Article

# A 3 mm Spectral Line Study of the Central Molecular Zone Infrared Dark Cloud G1.75-0.08

Oskari Miettinen <sup>1,\*</sup>  and Miguel Santander-García <sup>2,3</sup> 

<sup>1</sup> Research Council of Finland, Hakaniemenranta 6, P.O. Box 131, FI-00531 Helsinki, Finland

<sup>2</sup> Observatorio Astronómico Nacional (OAN-IGN), Alfonso XII, 3, 28014 Madrid, Spain; m.santander@oan.es

<sup>3</sup> Centro de Desarrollos Tecnológicos, Observatorio de Yebes (IGN), 19141 Yebes, Guadalajara, Spain

\* Correspondence: oskari.miettinen@aka.fi

**Abstract:** Infrared dark clouds (IRDCs) are fruitful objects to study the fragmentation of interstellar filaments and initial conditions and early stages of high-mass ( $M > 8 M_{\odot}$ ) star formation. We used the Yebes 40 m and Institut de Radioastronomie Millimétrique (IRAM) 30 m radio telescopes to carry out the first single-pointing spectral line observations towards the IRDC G1.75-0.08, which is a filamentary Central Molecular Zone (CMZ) cloud. Our aim is to reach an improved understanding of the gas kinematics and dynamical state of the cloud and its two clumps that we call clumps A and B. We also aim to determine the fractional abundances of the molecules detected at 3 mm towards G1.75-0.08. We detected HNC( $J_{K_a, K_c} = 4_{0,4} - 3_{0,3}$ ), HCN( $J = 1 - 0$ ), and HCO<sup>+</sup>( $J = 1 - 0$ ) towards both clumps. The N<sub>2</sub>H<sup>+</sup>( $J = 1 - 0$ ) line was detected only in clump B, while N<sub>2</sub>D<sup>+</sup>( $J = 1 - 0$ ) was not detected at all. The HCN and HNC spectra exhibit two velocity components. The abundances of the detected species are comparable to those in other IRDCs. An upper limit to the [N<sub>2</sub>D<sup>+</sup>]/[N<sub>2</sub>H<sup>+</sup>] deuterium fraction of  $< 0.05$  derived towards clump B is consistent with values observed in many high-mass clumps. The line mass analysis suggests that the G1.75-0.08 filament is subcritical by a factor of  $11 \pm 6$ , and the clumps were found to be gravitationally unbound ( $\alpha_{\text{vir}} > 2$ ). Our finding that G1.75-0.08 is strongly subcritical is atypical compared to the general population of Galactic filamentary clouds. The cloud's location in the CMZ might affect the cloud kinematics similar to what has been found for the Brick IRDC, and the cloud's dynamical state might also be the result of the turbulent motions or shear and tidal forces in the CMZ. Because the target clumps are dark at 70  $\mu\text{m}$  and massive (several  $10^3 M_{\odot}$ ), they can be considered candidates for being high-mass starless clumps but not prestellar because they are not gravitationally bound.

**Keywords:** astrochemistry; line: profiles; ISM: clouds; ISM: individual objects: G1.75-0.08; ISM: kinematics and dynamics

## 1. Introduction

Interstellar infrared dark clouds (IRDCs) are identified as dark absorption features against the Galactic mid-IR background radiation (e.g., [1–3]). Infrared dark clouds are very useful target sources for the studies of molecular cloud fragmentation and star formation. One reason for this is that IRDCs often exhibit filamentary morphology with substructure along the long axis of the filament (e.g., [4–7]). Another reason for IRDCs being useful target sources is that some of them show evidence of ongoing high-mass ( $M > 8 M_{\odot}$ ) star formation (e.g., [8–12]), a process where many details and even the exact mechanism(s) are still to be deciphered (e.g., [13] for a review). On the other hand, IRDCs are promising sites to search for high-mass prestellar clumps and cores (e.g., [14]).

In this paper, we present a molecular spectral line study of the Galactic IRDC G1.75-0.08 (Figure 1). The target IRDC was uncovered by dust continuum imaging survey with the Large APEX Bolometer Camera (LABOCA; [15]) at 870  $\mu\text{m}$  by Miettinen [16], and it was part of the sample in the molecular line study of IRDCs by Miettinen [17] that was based

arXiv:2406.18478v1 [astro-ph.GA] 26 Jun 2024



**Citation:** Miettinen, O.; Santander-García, M. A 3 mm Spectral Line Study of the Central Molecular Zone Infrared Dark Cloud G1.75-0.08. *Galaxies* **2024**, *1*, 0. <https://doi.org/>

Received:  
Revised:  
Accepted:  
Published:



**Copyright:** © 2024 by the authors. Licensee MDPI, Basel, Switzerland. This article is an open access article distributed under the terms and conditions of the Creative Commons Attribution (CC BY) license (<https://creativecommons.org/licenses/by/4.0/>).

on the Millimetre Astronomy Legacy Team 90 GHz (MALT90) survey [18–20]. A follow-up dust continuum imaging study of G1.75-0.08 at 350  $\mu\text{m}$  and 450  $\mu\text{m}$  was conducted by Miettinen et al. [21] using the Architectures de bolomètres pour des Télescopes à grand champ de vue dans le domaine sub-Millimétrique au Sol, or ArTéMiS bolometer [22–24]. Miettinen et al. [21] revised the kinematic distance of G1.75-0.08 to be 8.22 kpc with a Galactocentric distance of 270 pc. Hence, G1.75-0.08 is located within the Central Molecular Zone (CMZ) of the Galaxy, where the cloud can be associated with extreme environmental conditions such as strong tidal shear forces, strong turbulence, and more complex chemistry than found in the Galactic spiral arm molecular clouds (e.g., [25]; see also [26] for a review).

Prior to the present study, the only spectral line data available for G1.75-0.08 were those obtained as part of the MALT90 survey. The modest sensitivity of the MALT90 data ( $\sim 250$  mK per  $0.11$  km s $^{-1}$  channel) and the angular resolution (half-power beam width, or HPBW) of those data, 38 arcsec, complicated the interpretation of the few extracted line detections (e.g., HCN( $J = 1 - 0$ ) and HCO $^+$ ( $J = 1 - 0$ ); [17]). Our new spectral line observations with the Yebes 40 m telescope benefit from 1.9 times higher angular resolution compared to the MALT90 data, which is useful owing to the large distance of the cloud from the Sun. In the present paper, we will revise some of the source properties that depend on information provided by spectral line data (in particular, spectral line widths), and determine the fractional abundances of the molecules detected towards the target source via our 3 mm band observations.

The observations and data reduction are described in Section 2. The analysis and results are described in Section 3. We discuss the results in Section 4, while in Section 5, we summarise our results and main conclusions.

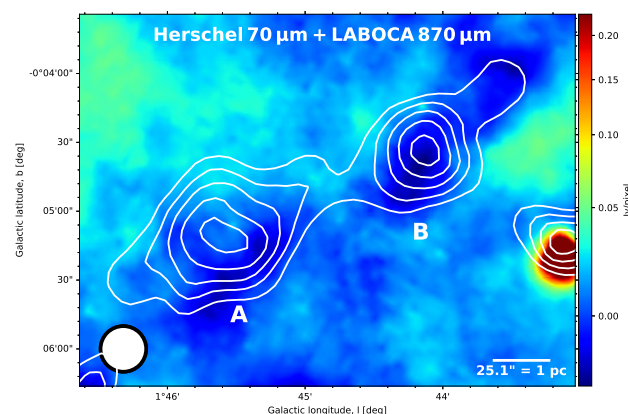


**Figure 1.** *Herschel* 70  $\mu\text{m}$  image towards G1.75-0.08 (colour map) overlaid with contours showing the LABOCA 870  $\mu\text{m}$  emission. The contour levels start from  $3\sigma$  and progress in steps of  $1\sigma$ , where  $1\sigma = 90$  mJy beam $^{-1}$ . The two clumps, clump A and clump B, are labelled A and B. The beam size (HPBW of 19.9 arcsec) of the LABOCA observations is shown in the bottom left corner and a scale bar of 1 pc is shown in the bottom right corner.

## 2. Observations and Data Reduction

### 2.1. Yebes Observations

We used the Yebes 40 m radio telescope [27] to observe the LABOCA 870  $\mu\text{m}$  peak positions of the clumps in G1.75-0.08 at a frequency range of about 72–90.5 GHz. The observed frequency was tuned at 80.05 GHz. The target clumps are listed in Table 1.

Our observations made use of the W band, where the full bandwidth is 18.5 GHz. The spectral backend was a Fast-Fourier Transform Spectrometer (FFTS) with a spectral resolution of 38 kHz, and the observations were made in dual (horizontal and vertical) linear polarisation mode. The aforementioned spectral resolution corresponds to a velocity resolution of 126–158.3 m s $^{-1}$  over the observed frequency range. The beam size (HPBW) at the observed frequency range is 19.5–24.5 arcsec ([27], Table 5 therein).

**Table 1.** Target clumps in G1.75-0.08.

Source	$\alpha_{2000.0}$ [h:m:s]	$\delta_{2000.0}$ [°:':"]	$T_{\text{dust}}$ [K]	$M$ [ $M_{\odot}$ ]
Clump A	17 50 05.08	−27 28 32.12	$14.3 \pm 0.4$	$5501 \pm 935$
Clump B	17 49 59.38	−27 29 24.98	$14.5 \pm 0.5$	$3770 \pm 738$

The columns are as follows: (1) source name; (2) and (3) coordinates of the LABOCA 870  $\mu\text{m}$  peak surface brightness position; (4) dust temperature; (5) total (gas+dust) mass of the clump. The values of  $T_{\text{dust}}$  and  $M$  were derived by Miettinen et al. [21].

The first observations were carried out on 27 and 28 March 2023 (for clump B and clump A, respectively) under the project 23A004 (PI: Miettinen). These observations were performed in the position switching mode, where the off position for clump A was 1.092 arcmin to the north of the on position, and for clump B, the reference position was located at 0.874 arcmins to the north of the target position. These offsets were chosen on the basis of the extent of the LABOCA 870  $\mu\text{m}$  emission (Figure 1). The total on-source integration time for clump A was 31 min, and for clump B, it was about 21 min. However, it was found that the reference off positions of the observations had spectral line emission at the observed frequencies, which resulted in absorption-like features in the final spectra that corrupted the lines observed towards the on positions.

The observations were repeated on 11 and 16 February 2024 (for clump A and clump B, respectively) under project 24A005 (PI: Miettinen). These observations were performed in the frequency switching mode with a conservative frequency throw of 74.1 MHz ( $\pm 37.05$  MHz frequency offsets). Because, in the frequency switching mode, the observed position does not change, we could avoid the possible presence of spectral line emission in the position switching mode's reference position. The pointing and focus corrections were conducted by observing a SiO maser line at 86,243.4277 MHz towards the Red Supergiant VX Sgr. The total on-source integration time for clump A was 1.15 h, and for clump B, it was 1.9 h.

The system temperature during the observations towards clump A was  $T_{\text{sys}} \simeq 200$  K, while for observations of clump B, it was about 300 K. Calibration was made by the hot-cold load technique, and the output intensity scale given by the system is the antenna temperature corrected for the atmospheric attenuation ( $T_{\text{A}}^*$ ). The observed intensities were converted to the main-beam brightness temperature scale using the formula  $T_{\text{MB}} = T_{\text{A}}^* / \eta_{\text{MB}}$ , where  $\eta_{\text{MB}}$  is the main-beam efficiency. The values of  $\eta_{\text{MB}}$  range from 0.20 to 0.31 over the observed frequency range.<sup>1</sup> The absolute calibration uncertainty was adopted to be 10% following the practice of studies that employ the Yebes Q-band observations (e.g., [28–30]). However, this should be taken as a lower limit to the calibration uncertainty in the higher frequency W band. Moreover, it has been observed that the spectral line intensity discrepancies between position and frequency switching observations with the Yebes 40 m radio telescope are always  $< 20\%$  [27].

The spectra were reduced using Continuum and Line Analysis Single-dish Software (CLASS90) of the GILDAS software package (version jul21)<sup>2</sup>. The individual spectra were stitched with weights defined as  $w_i \propto t_{\text{int}} / T_{\text{sys}}^2$ , where  $t_{\text{int}}$  is the integration time. The resulting spectra were folded and then smoothed using the Hann window function so that the number of channels was divided by two. First or second-order baselines were determined from the velocity ranges free of spectral line features and then subtracted from the spectra. The resulting  $1\sigma$  rms noise levels at the smoothed velocity resolution were about 20–33 mK with an average of 26.6 mK on a  $T_{\text{A}}^*$  scale.

## 2.2. IRAM Observations

We also used the Institut de Radioastronomie Millimétrique (IRAM) 30 m telescope to observe the target positions (i.e., the LABOCA 870  $\mu\text{m}$  peaks of the clumps) in the  $J = 1 - 0$  transition of  $\text{N}_2\text{H}^+$  and  $\text{N}_2\text{D}^+$ . The observations were carried out on 8 and 14 February 2024 during a pool observing week (project 079-23; PI: Miettinen).

The Eight Mixer Receiver (EMIR; [31]) band E090 was used as a front end, while the backend was the Versatile Spectrometer Array (VESPA), where the bandwidth was  $18 \times 20$  MHz with a corresponding channel spacing of 20 kHz. The  $\text{N}_2\text{H}^+(1-0)$  and  $\text{N}_2\text{D}^+(1-0)$  lines were tuned at the frequencies of the strongest hyperfine component ( $J_{F_1, F_2} = 1_{2,3} - 0_{1,2}$ ) of the transition, which are 93,173.7637 MHz and 77,109.6162 MHz, respectively, ([32], Tables 2 and 8 therein).

The aforementioned channel spacing yielded a velocity resolution of about  $64 \text{ m s}^{-1}$  for  $\text{N}_2\text{H}^+$  and  $78 \text{ m s}^{-1}$  for  $\text{N}_2\text{D}^+$ . The telescope beam sizes (HPBW) at the observed frequencies are 26.4 arcsec ( $\text{N}_2\text{H}^+$ ) and 31.9 arcsec ( $\text{N}_2\text{D}^+$ ).

The observations were performed in the frequency switching mode with a frequency throw of  $\pm 3.9$  MHz. The  $\text{N}_2\text{H}^+(1-0)$  observing time for both clumps was about 1.1 h. The  $\text{N}_2\text{D}^+(1-0)$  observing time for clump A was 2.2 h and 1.6 h for clump B. The telescope focus and pointing were optimised and checked on the quasars 1226+023 (3C 273) and 1757-240. The precipitable water vapour (PWV) during the observations was measured to be between 4.2 mm and 5.5 mm. The system temperatures during the observations were within the range of  $T_{\text{sys}} = 113 - 140$  K. The observed intensities were converted into the main-beam brightness temperature scale by using a main-beam efficiency factor of  $\eta_{\text{MB}} = 0.80$  for  $\text{N}_2\text{H}^+(1-0)$  and 0.81 for  $\text{N}_2\text{D}^+(1-0)$ . The absolute calibration uncertainty was adopted to be 10% (e.g., [33]).

The spectra were reduced using CLASS90 (version jul21) in a similar fashion as described in Section 2.1 (including smoothing that halves the spectral resolution). Second- or third-order polynomial baselines were determined from the velocity ranges free of spectral line features, and then subtracted from the spectra. The resulting  $1\sigma$  rms noise levels were about 13–21 mK.

### 3. Analysis and Results

#### 3.1. Detected Spectral Lines and Spectral Line Parameters

To identify the spectral lines in the W band observed with the Yebes telescope, we made use of the Splatologue interface<sup>3</sup>, and the Cologne Database for Molecular Spectroscopy (CDMS<sup>4</sup>; [34]) and the Jet Propulsion Laboratory (JPL) spectroscopic database<sup>5</sup> [35]. The spectra of the spectral line transitions detected with Yebes towards both target clumps are shown in Figures 2 and 3. The spectra observed with the IRAM 30 m telescope are shown in Figure 4. The detected spectral line transitions are listed in Table 2. As can be seen in Figures 2 and 3, the Yebes spectra exhibit wavy baseline structures that could not be described by simple first- or second-order baseline functions. Wavy baselines can be the result of frequency switching that we employed in our Yebes observations (e.g., [36,37]).

As shown in Figures 2 and 3, the  $\text{HCO}^+$  lines were fitted by a single Gaussian function using CLASS90 (version jul21). The HCN lines exhibit hyperfine splitting (three components in the case of the  $J = 1 - 0$  transition; e.g., [38]), and we used the hyperfine structure method of CLASS90 to fit the detected lines. Owing to the detected HCN line profiles, the fitting was conducted using a two-velocity component model. One could also interpret the observed HCN line profiles as asymmetric, where the redshifted peak is stronger than the blueshifted peak and where there is a self-absorption dip between the two peaks. This, however, would require that an optically thin line emission is seen at a velocity of about  $27 \text{ km s}^{-1}$  (estimated from the HCN spectrum towards clump A), which is lower than the systemic local standard of rest (LSR) velocity of the cloud ( $\sim 50 \text{ km s}^{-1}$ ).

The HNCO lines also exhibit a hyperfine structure (e.g., [39]), and the observed  $J = 4 - 3$  transition has six hyperfine components. The detected HNCO lines were fit using the hyperfine structure method and hyperfine component frequencies from the CDMS database. Again, the fitting was made using two velocity components. Similar to the case of HCN, the HNCO line detected towards clump A could also be interpreted as a red asymmetric line profile with a central dip at about  $36 \text{ km s}^{-1}$ .

We note that our original aim was also to observe the DCN( $J = 1 - 0$ ) transition at 72.415 GHz towards the target clumps (to study the [DCN]/[HCN] deuteration), but the observed spectra had a very strong wave-like structure between about 72 and 76 GHz, which prevented any potential detection of the line.

The only line detected in our IRAM 30 m telescope observations is  $N_2H^+(1 - 0)$  towards clump B. Even this detection is relatively weak ( $\sim 6\sigma$ ) compared to the lines detected with Yebes. The  $J = 1 - 0$  transition of  $N_2H^+$  is split into 15 hyperfine components, which are mostly blended into one broad line in the observed spectra with a hint of a blended group at  $\sim 40$  km s $^{-1}$ . We fitted the hyperfine structure in CLASS90 using the rest frequencies from [32] (Table 2 therein) and the relative intensities from [40] (Table 8 therein).

The derived basic line parameters are listed in columns 2–5 in Table 3. Besides the formal  $1\sigma$  fitting errors output by CLASS90, the errors in the peak intensity ( $T_{MB}$ ) and the integrated intensity of the line ( $\int T_{MB}dv$ ) also include the 10% calibration uncertainty (the two sources of uncertainty were added in quadrature). We note that the quoted uncertainties in  $\int T_{MB}dv$  should be interpreted as lower limits only because of the blended velocity components and ripples in the observed spectra.

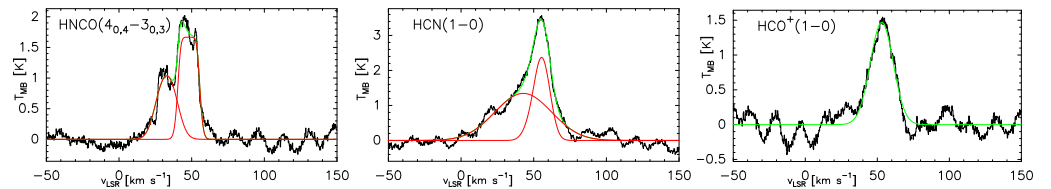


**Figure 2.** Spectral lines detected with the Yebes telescope towards clump A. Hyperfine structure fits to the two velocity components in the HNC and HCN spectra are shown in red, while the green line shows the sum of the two components. A single Gaussian fit to the  $HCO^+$  line is overlaid in green. The intensity range in the panels differs from each other to better show the line profiles.

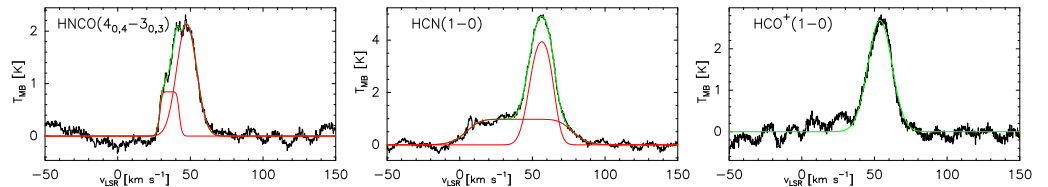


**Figure 3.** Same as Figure 2 but for clump B.

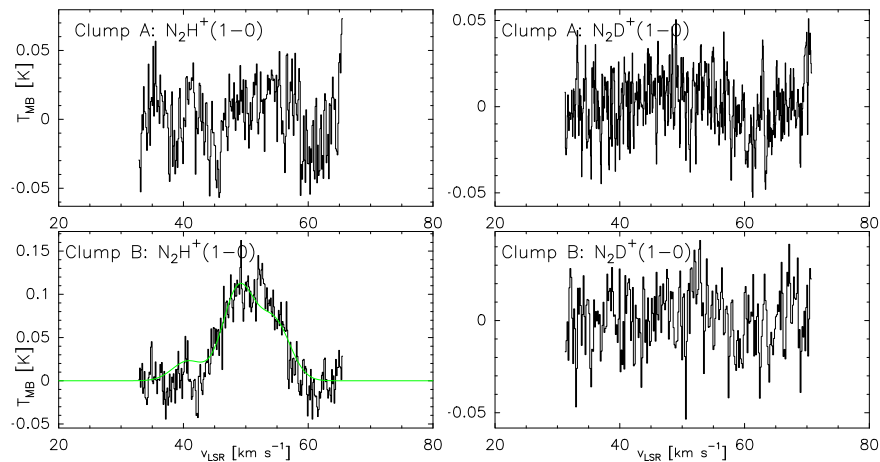


**Figure 4.** The spectra observed with the IRAM 30 m telescope. The only detection is  $N_2H^+(1 - 0)$  towards clump B, where the hyperfine structure fit is shown in green. The velocity range in the panels is different from that in Figures 2 and 3 because of the narrower frequency bands used in the IRAM 30 m/VESPA observations.

**Table 2.** Detected spectral lines.

Transition	$\nu$ [MHz]	$E_u/k_B$ [K]	Telescope
HNCO( $J_{K_a, K_c} = 4_{0,4} - 3_{0,3}$ )	87 925.2178 <sup>a</sup>	10.55	Yebes
HCN( $J = 1 - 0$ )	88 631.846 <sup>b</sup>	4.25	Yebes
HCO <sup>+</sup> ( $J = 1 - 0$ )	89 188.5247	4.28	Yebes
N <sub>2</sub> H <sup>+</sup> ( $J = 1 - 0$ )	93 173.7637 <sup>c</sup>	4.47	IRAM 30 m

The spectroscopic data were compiled from the CDMS database unless otherwise stated. In columns 2 and 3, we list the line rest frequency and the upper-state energy divided by the Boltzmann constant. <sup>a</sup> Frequency of the strongest hyperfine component  $F = 5 - 4$  (relative intensity  $R_i = 0.4074$ ). <sup>b</sup> Frequency of the strongest hyperfine component  $F = 2 - 1$  (relative intensity  $R_i = 0.5555$ ) taken from Loughnane et al. [38]. <sup>c</sup> Frequency of the strongest hyperfine component  $F_1, F = 2, 3 - 1, 2$  (relative intensity  $R_i(F_1, J)R_i(F, F_1) = 7/27$ ; [40]) taken from [32].

### 3.2. Line Optical Thicknesses and Excitation Temperatures

If a spectral line transition is split into hyperfine components, the relative strengths of the hyperfine components can be used to derive the line optical thickness,  $\tau$ . However, in all cases where we fit the hyperfine structure of the line (Section 3.1), the hyperfine structure was not resolved (i.e., the separate components are blended), and hence, the corresponding optical thicknesses should be taken with caution. When the optical thickness could be estimated by the CLASS90 routine, the corresponding excitation temperature of the line was calculated using Equation (1) in Miettinen [41].

For HCO<sup>+</sup>, we assumed that the rotational transition is thermalised at the dust temperature of the clump; that is, we assumed that  $T_{\text{ex}} = T_{\text{dust}}$  (see column 4 in Table 1). The values of  $\tau$  and  $T_{\text{ex}}$  are listed in columns 6 and 7 in Table 3.

**Table 3.** Spectral line parameters of the detected transitions and molecular column densities and fractional abundances.

Transition	$v_{\text{LSR}}$ [km s <sup>-1</sup> ]	$\Delta\nu$ [km s <sup>-1</sup> ]	$T_{\text{MB}}$ [K]	$\int T_{\text{MB}} d\nu$ [K km s <sup>-1</sup> ]	$\tau$	$T_{\text{ex}}$ [K]	$N$ [cm <sup>-2</sup> ]	$x$
Clump A								
HNCO( $4_{0,4} - 3_{0,3}$ )	47.80 ± 0.11	8.28 ± 0.26	1.72 ± 0.17	35.09 ± 3.53	7.64 ± 0.97	4.7 ± 0.2	4.9 ± 0.6(14)	8.8 ± 1.8(-9)
	32.10 ± 0.28	14.60 ± 0.69	0.99 ± 0.10	9.34 ± 1.00	0.12 ± 0.01	23.9 ± 2.7	1.9 ± 0.2(14)	...
HCN(1 - 0)	54.10 ± 0.09	10.90 ± 0.35	2.37 ± 0.24	35.07 ± 3.55	0.11 ± 0.01	43.2 ± 5.4	2.5 ± 0.2(14)	4.5 ± 0.8(-9)
	42.00 ± 0.42	43.90 ± 0.83	1.36 ± 0.14	64.31 ± 6.40	0.14 ± 0.05	21.4 ± 6.5	3.4 ± 1.2(14)	...
HCO <sup>+</sup> (1 - 0)	53.10 ± 0.16	18.75 ± 0.37	1.47 ± 0.15	29.31 ± 2.97	0.14 ± 0.01 <sup>a</sup>	14.3 ± 0.4	5.2 ± 0.2(13)	9.3 ± 1.5(-10)
Clump B								
HNCO( $4_{0,4} - 3_{0,3}$ )	47.40 ± 0.11	14.70 ± 0.29	2.00 ± 0.20	33.36 ± 4.96	0.57 ± 0.04	12.8 ± 1.1	2.6 ± 0.2(14)	4.9 ± 0.9(-9)
	35.50 ± 0.04	6.61 ± 0.15	1.10 ± 0.11	14.66 ± 3.88	11.20 ± 0.81	4.0 ± 0.1	5.2 ± 0.4(14)	...
HCN(1 - 0)	55.20 ± 0.04	11.90 ± 0.28	3.88 ± 0.39	79.85 ± 8.05	1.79 ± 0.18	9.3 ± 0.7	2.6 ± 0.3(14)	4.9 ± 0.9(-9)
	40.40 ± 0.24	36.70 ± 0.23	1.10 ± 0.11	68.06 ± 6.90	10.30 ± 0.13	4.0 ± 0.1	1.2 ± 0.1(15)	...
HCO <sup>+</sup> (1 - 0)	53.80 ± 0.07	19.39 ± 0.18	2.69 ± 0.27	55.49 ± 5.57	0.27 ± 0.02 <sup>a</sup>	14.5 ± 0.5	1.1 ± 0.1(14)	2.0 ± 0.3(-9)
N <sub>2</sub> H <sup>+</sup> (1 - 0)	48.70 ± 0.12	5.79 ± 0.21	0.12 ± 0.02	1.14 ± 0.11	0.10 ± 0.05	7.8 ± 2.5	4.2 ± 0.6(12)	7.9 ± 1.7(-11)

Columns 2–9 give the LSR radial velocity ( $v_{\text{LSR}}$ ), full width at half maximum (FWHM;  $\Delta\nu$ ), peak intensity ( $T_{\text{MB}}$ ), integrated intensity ( $\int T_{\text{MB}} d\nu$ ), optical thickness ( $\tau$ ), excitation temperature ( $T_{\text{ex}}$ ) of the line, and the molecule's beam-averaged column density and fractional abundance with respect to H<sub>2</sub>. The latter two quantities are given in the form  $a \pm b(c)$ , which stands for  $(a \pm b) \times 10^c$ . <sup>a</sup> The optical thickness was calculated under the assumption that  $T_{\text{ex}} = T_{\text{dust}}$  (Section 3.2).

### 3.3. Molecular Column Densities and Fractional Abundances

To calculate the beam-averaged column densities of the molecules, we used the standard local thermodynamic equilibrium (LTE) approach (see Equation (32) in [40])<sup>6</sup>.

The values of the product  $\mu^2 S$  were taken from the Splatalogue accessed CDMS database. The rotational degeneracy ( $g_J$ ) was calculated from the rotational quantum number of the upper state (see Equation (34) in [40]). HNCO is an asymmetric top molecule and its  $K$ -level and reduced nuclear spin degeneracies ( $g_K$  and  $g_I$ ) were assigned values

following the rules in Turner [42] (see Appendix therein). The value of  $g_K$  equals 1 for asymmetric tops, and the value of  $g_I$  for HNC is also 1 because the molecule has no identical interchangeable nuclei. The partition functions were calculated using Equations (3) and (4) in Miettinen [17].

The fractional abundances of the molecules were calculated by dividing the molecular column density by the  $H_2$  column density. The  $H_2$  column densities of the clumps were calculated from the LABOCA 870  $\mu\text{m}$  peak surfaces brightness and using the dust temperature given in column 4 in Table 1 (see, e.g., Equation (6) in [41]). We assumed that the mean molecular weight per  $H_2$  molecule is  $\mu_{H_2} = 2.82$ , the dust opacity is  $\kappa_{870 \mu\text{m}} = 1.38 \text{ cm}^2 \text{ g}^{-1}$  at 870  $\mu\text{m}$ , and the dust-to-gas mass ratio is  $R_{d/g} = 1/141$  (see [41] and references therein). The angular resolution of our LABOCA data,  $\sim 20$  arcsec, is very similar to the Yebes 40 m telescope angular resolution at the frequency of the analysed spectral lines (i.e., 19.7–20 arcsec), and also comparable to the IRAM 30 m telescope beam size (26.4 arcsec). Hence, no smoothing of the LABOCA data was performed for calculating the  $H_2$  column densities. The beam-averaged column densities and fractional abundances of the molecules with respect to  $H_2$  are listed in the last two columns in Table 3. The fractional abundance is only calculated for the main velocity component under the assumption that the observed submillimetre dust emission originates only in the target cloud.

### 3.4. Virial Analysis of the Cloud and Its Clumps

Miettinen et al. [21] derived a line mass of  $1011 \pm 146 M_\odot \text{ pc}^{-1}$  for the G1.75-0.08 filament. The present spectral line data allow us to revise the virial or critical line mass of the cloud (see, e.g., Equation (12) in [43]). To calculate the latter quantity, we used the total (thermal+non-thermal) velocity dispersion, where the observed spectral line width (FWHM) was taken to be the average of the FWHMs of the HNC lines detected towards clump A and clump B, because (i) the transition has a high critical density ( $10^6 \text{ cm}^{-3}$  at 20 K; [44], Table 1 therein), (ii) the detected lines do not exhibit as strong wing emission as the HCN lines, and (iii) HNC was detected towards both clumps. The value of the aforementioned average FWHM is  $11.5 \pm 3.2 \text{ km s}^{-1}$ . We assumed that the gas kinetic temperature is equal to the dust temperature ( $15.0 \pm 0.4 \text{ K}$  for the filament; [21]). The derived virial line mass and the ratio of the observed and virial line masses are listed in Table 4.

We also revised the virial masses and virial parameters (the ratio of the virial mass to the source mass) of the target clumps derived by Miettinen et al. [21] (see Section 3.5 therein). For this purpose, we also employed the HNC line widths. It was again assumed that the gas temperature is equal to the dust temperature. The clumps were assumed to have a radial density profile of the form  $n(r) \propto r^{-1.6}$ , which is consistent with those derived for Galactic high-mass star-forming clumps (see [45] and references therein). The power-law index of the density profile,  $p$ , modifies the virial mass as  $M_{\text{vir}} \propto a^{-1}$ , where  $a = (1 - p/3)/(1 - 2p/5)$  (see [46] and references therein). The mean molecular weight per free particle was assumed to be  $\mu_p = 2.37$ . The derived virial masses and virial parameters of the clumps are listed in Table 4.

**Table 4.** Virial masses and virial parameters of the target sources.

Source	$M_{\text{vir}}$	$\alpha_{\text{vir}}^a$
G1.75-0.08	$11,113 \pm 6171 M_\odot \text{ pc}^{-1}{}^b$	$0.09 \pm 0.05$
Clump A	$16,248 \pm 1017 M_\odot$	$3.0 \pm 0.5$
Clump B	$43,384 \pm 1710 M_\odot$	$11.5 \pm 2.3$

<sup>a</sup> For the G1.75-0.08 filament, the virial parameter is defined as the ratio of the line mass to virial line mass, while for the clumps the virial parameter is defined the other way round, that is, as the ratio of the virial mass to the clump mass. <sup>b</sup> Virial or critical line mass.

## 4. Discussion

### 4.1. Spectral line Profiles and Cloud Kinematics

The HCN and HNCO lines we detected towards the clumps of G1.75-0.08 show asymmetric profiles that we have interpreted to be caused by two different velocity components (see Figures 2 and 3). The presence of multiple nearby velocity components complicates the interpretation of the gas kinematics of the cloud. In principle, the detected red asymmetric line profiles could also be indicative of outward motions or cloud expansion (e.g., [47–50]). For this to be the case, however, we should see optically thin line emission at a systemic velocity that matches the velocity of the central dip, which is not the case. Hence, the presence of multiple different velocity components seems more likely. Indeed, physically unassociated clouds along the line of sight that have different LSR velocities would not be unexpected owing to the large distance of G1.75-0.08. However, this needs to be tested by further spectral line observations.

The HCN(1 – 0) spectrum extracted towards the LABOCA peak position of clump A by Miettinen [17] also showed a hint of a red asymmetric profile (see Figure C.6 therein).<sup>7</sup> The HNCO(4<sub>0,4</sub> – 3<sub>0,3</sub>) line detected by Miettinen [17] towards clump A was interpreted as a single, very broad line ( $30.40 \pm 1.39$  km s<sup>-1</sup> in FWHM), but our 1.9 times higher angular resolution and more sensitive observations have revealed the presence of two velocity components. The HCO<sup>+</sup>(1 – 0) spectrum towards clump A in Miettinen [17] was interpreted to exhibit two velocity components, while in the present study the line appears to have only one clear velocity component. The larger beam of the MALT90 observations (38 arcsec) might have captured emission from another velocity component that is now avoided. However, the potential presence of an additional component at  $\sim 30$  km s<sup>-1</sup> is blurred by the rippled baseline in the HCO<sup>+</sup>(1 – 0) spectrum.

All the MALT90 spectra towards clump B in Miettinen [17] were detected to have only one velocity component (see Figure C.2 therein). The difference compared to the present results is most notable for HCN, where we now see a broad ( $36.70 \pm 0.23$  km s<sup>-1</sup> in FWHM) secondary component. The HNCO line we detected with Yebes, however, could have been interpreted to have a single-velocity component as conducted by Miettinen [17], but in that case, the radial velocity of the line would have been lower ( $44.5$  km s<sup>-1</sup>) than that derived for the stronger peak in the HCN spectrum ( $55.2$  km s<sup>-1</sup>), which presumably originates in our target cloud. The N<sub>2</sub>H<sup>+</sup>(1 – 0) line towards clump B analysed in Miettinen [17] was derived from having an FWHM of  $20.10 \pm 1.69$  km s<sup>-1</sup>, which is  $3.5 \pm 0.3$  broader than derived in the present study. In this case, the larger beam of the MALT90 observations might have captured emission from gas with higher velocity dispersion than probed by our new IRAM observations.

Miettinen et al. [21] speculated that G1.75-0.08 might represent a case where a filamentary cloud is undergoing gravitational focussing or the so-called edge effect, where gas clumps have accumulated at both ends of the filament (e.g., [51–54]). It would be tempting to interpret the detected HCN and HNCO line profiles as red asymmetric lines that indicate the presence of outward gas motions, because this might support the hypothesis of gravitational focussing. However, further spectral line observations are needed to test this hypothesis.

CMZ clouds can have a complex velocity field, as was demonstrated by Henshaw et al. [55] in the case of the CMZ cloud G0.253+0.016 (also known as the Brick). Henshaw et al. [55] found that the Brick is not a single, coherent cloud, but rather a structured system of different velocity components and complex dynamics that might be the result of the orbital dynamics and shear motions in the CMZ. On the basis of the present results, G1.75-0.08 could be an analogue object with the Brick. High angular and spectral resolution imaging of G1.75-0.08 would, however, be required to reach a better understanding of the velocity structure of the cloud.

#### 4.2. Dynamical State of G1.75-0.08

Using the HCN(1 – 0) line width (FWHM) of  $13.50 \pm 0.38 \text{ km s}^{-1}$  detected in the MALT90 survey, Miettinen et al. [21] derived a low value of  $0.07 \pm 0.01$  for the ratio of the line mass to the critical line mass for G1.75-0.08. In the present paper, we have used our new molecular line data (specifically HNC line widths) to revise the latter value to  $0.09 \pm 0.05$  (Table 4), which is very close to the earlier estimate. Hence, our finding supports the view that G1.75-0.08 is strongly subcritical (by a factor of  $11 \pm 6$ ), which makes it very different compared to the general population of Galactic filaments for which the line mass and the critical line mass are often found to agree within a factor of  $\sim 2$  (e.g., [56]; Figure 27 therein). One could speculate that G1.75-0.08 is subject to tidal disruption effects near the Galactic Centre ( $R_{GC} \sim 270 \text{ pc}$ ; [21]). The dynamical CMZ environment is found to have an influence on the Brick [55], and hence, this might be the case for G1.75-0.08 as well.

We note that if the FWHM of  $\text{N}_2\text{H}^+(1 - 0)$  detected towards clump B would be used in the analysis, the virial parameter for G1.75-0.08 would become  $\alpha_{\text{vir}}^{\text{fil}} = 0.36 \pm 0.06$ , in which case the filament would be subcritical only by a factor of  $2.8 \pm 0.5$ . However,  $\text{N}_2\text{H}^+(1 - 0)$  is detected only in clump B, and the detection is relatively weak compared to other line detections; hence, the corresponding line FWHM might not be as reliable as for HNC used in the analysis.

#### 4.3. Dynamical State of the Clumps

Our new molecular line data also allowed us to revise the virial parameters of the clumps in G1.75-0.08. Miettinen et al. [21] found that clumps A and B are both gravitationally unbound with  $\alpha_{\text{vir}} \gg 2$  (see Table 7 therein). Our new data support the conclusion that the clumps are gravitationally unbound ( $\alpha_{\text{vir}} > 2$ ; Table 4), although clump A lies only a factor of  $1.5 \pm 0.3$  away from being gravitationally bound.

We note that if the FWHM of  $\text{N}_2\text{H}^+(1 - 0)$  detected towards clump B would be used in the calculation, the virial parameter of clump B would become  $\alpha_{\text{vir}} = 1.8 \pm 0.4$ , which would suggest that the clump is marginally gravitationally bound. However, as noted in Section 4.2, the  $\text{N}_2\text{H}^+(1 - 0)$  detection towards clump B is relatively weak and the corresponding line FWHM should be interpreted with caution. It should also be noted that further support against gravity is provided by a magnetic field, and the magnetic field strength in the CMZ is known to be relatively strong compared to molecular clouds at larger Galactocentric distances (e.g., [57]).

The clumps appear dark at  $70 \mu\text{m}$  and lie above the mass–radius threshold for high-mass star formation proposed by Baleschi et al. [58], as shown in Figure 7 of a study by Miettinen et al. [21], and which is given by  $M_{\text{thresh}} = 1732 M_{\odot} \times (R/\text{pc})^{1.42}$  when scaled to our assumptions about the dust opacity and gas-to-dust mass ratio [45]. However, the present data do not suggest the clumps to be candidates for being high-mass prestellar clumps, but only high-mass starless clumps. Moreover,  $70 \mu\text{m}$  darkness does not necessarily mean that the clump is quiescent or devoid of star formation, and such objects can host embedded low- and intermediate-mass protostellar cores (e.g., [59–61]). For example, the line wing emission seen in our HCN and HNC spectra might arise from protostellar outflow activity. However, this is only speculation and requires high-resolution spectral line imaging to be confirmed or disproved. On the other hand, a deficit of gravitationally bound clumps in the CMZ could explain its low star formation rate (SFR) compared to the Galaxy in general [62]. Chabrier and Dumond [63] suggested that molecular clouds in the CMZ are subject to only one episode of large-scale turbulence injection during their lifetime, where the injection is mostly provided by the gas inflow driven by the Galactic bar. Hence, there can be less injection of turbulence and turbulent motion will eventually decay, which facilitates the formation of stars. This could then explain the low SFR compared to the Galactic disc. A low SFR in the CMZ may also be related to the tidal effects of the Galactic Centre.

Dust continuum imaging of G1.75-0.08 with ArTéMiS by Miettinen et al. [21] revealed that clumps A and B show substructure (see Figure 8 therein). Dense cores in gravitationally

unbound clumps have also been observed in other IRDCs (e.g., G340.222–00.167 with  $\alpha_{\text{vir}} = 5.7 \pm 1.7$ ; [64]). If the substructure detected with ArTéMiS is physical, it could be an indication that the inner parts of the clump have decoupled from the more turbulent outer parts of the clump and that gravitational fragmentation has taken place in the denser region within the parent clump.

The observed, projected separation of the substructures in the clumps is a factor of  $1.5 \pm 0.1$  larger than the thermal Jeans length for clump A and a factor of  $1.3 \pm 0.1$  larger in clump B (see Table 8 in [21]). Our new spectral line data (HNCO) suggest that the Jeans lengths that take the non-thermal motions into account would be larger by factors of about 10.5 (clump A) and 21 (clump B) than the observed substructure separation. Hence, the observed substructure in the clumps is roughly consistent with thermal Jeans fragmentation.

#### 4.4. Molecular Detections and Abundances in G1.75-0.08

##### 4.4.1. HNCO (Isocyanic Acid)

Based on the assumption that the higher velocity component of the HNCO line is associated with G1.75-0.08, we derived an HNCO fractional abundance of  $(8.8 \pm 1.8) \times 10^{-9}$  towards clump A and  $(4.9 \pm 0.9) \times 10^{-9}$  towards clump B.

For comparison, Vasyunina et al. [65], who used the 22 m Mopra telescope, detected the HNCO( $4_{0,4} - 3_{0,3}$ ) transition in 13 out of their sample of 37 clumps in 15 different IRDCs (35% detection rate), and derived abundances in the range of  $(0.17 - 2.86) \times 10^{-9}$ . The latter values were scaled down by a factor of 0.7735 to take the different assumptions used in the calculation into account (e.g., the dust opacity and dust-to-gas mass ratio), which is needed for a proper comparison with our results (see [41] for details). The abundances we derived towards our target clumps are  $3.1 \pm 0.6$  (clump A) and  $1.7 \pm 0.3$  (clump B) times higher than the highest value in the Vasyunina et al. [65] sample. We note that the distances of the Vasyunina et al. [65] target sources lie in the range of 2.1–5.3 kpc, and hence none of their sources are associated with the CMZ. Nevertheless, the HNCO abundances are not significantly different from those in G1.75-0.08.

Sanhueza et al. [44], who also used the 22 m Mopra telescope, detected HNCO( $4_{0,4} - 3_{0,3}$ ) in 18 of their sample of 92 clumps in IRDCs (20% detection rate), and derived abundances in the range of  $(0.15 - 4.45) \times 10^{-9}$ . The latter values were scaled down by a factor of 0.549 for a more meaningful comparison with our results (see [41]). The highest HNCO abundance in the Sanhueza et al. [44] sample is similar to that in clump B (agreement within a factor of  $1.1 \pm 0.2$ ).

We note that the HNCO( $4_{0,4} - 3_{0,3}$ ) line has also been detected in the Brick as part of the MALT90 survey [66] and also with the Atacama Large Millimetre/submillimetre Array (ALMA) [55,67], but no fractional abundance estimate was presented to compare with.

##### 4.4.2. HCN (Hydrogen Cyanide)

The HCN fractional abundances we derived for clump A and clump B are comparable to each other ( $(4.5 \pm 0.8) \times 10^{-9}$  and  $(4.9 \pm 0.9) \times 10^{-9}$ , respectively).

Vasyunina et al. [65] detected HCN( $1 - 0$ ) in all of their 37 clumps, and the scaled fractional abundances lie in the range of  $(0.26 - 5.26) \times 10^{-9}$ . The latter range brackets the HCN abundances we derived. Sanhueza et al. [44] also reported a high detection rate of HCN( $1 - 0$ ) for their sample (80%), but the fractional abundances were not derived owing to blended hyperfine components and complex line profiles.

##### 4.4.3. HCO<sup>+</sup> (Formyl Ion)

The HCO<sup>+</sup> abundance towards clump A was derived to be  $(9.3 \pm 1.5) \times 10^{-10}$ , while a value of  $(2.0 \pm 0.3) \times 10^{-9}$  was derived for clump B.

Vasyunina et al. [65] detected HCO<sup>+</sup>( $1 - 0$ ) in 31 clumps (83.8% detection rate), and the scaled fractional abundances lie in the range of  $(0.27 - 3.94) \times 10^{-8}$ . The lowest value in this range is  $2.9 \pm 0.5$  and  $1.4 \pm 0.2$  times higher than the abundance we derived

for clump A and clump B. Sanhueza et al. [44] reported a comparably high detection rate of  $\text{HCO}^+(1-0)$  for their sample (88%), and the scaled values of the fractional abundances lie in the range of  $(0.21 - 15.3) \times 10^{-8}$ . Again, the  $\text{HCO}^+$  abundance in our clumps is closer to the lower end of values in the Sanhueza et al. [44] sample. The authors found that the  $\text{HCO}^+$  abundance increases as the clump evolves, which in turn could be related to the increasing temperature, which leads to the release of CO from the icy grain mantles into the gas phase out of which  $\text{HCO}^+$  can then primarily form in the reaction with  $\text{H}_3^+$ . Because our target clumps are 70  $\mu\text{m}$  dark and apparently quiescent, their low  $\text{HCO}^+$  abundances are consistent with the aforementioned evolutionary trend.

#### 4.4.4. $\text{N}_2\text{H}^+$ (Diazenylium)

We detected  $\text{N}_2\text{H}^+$  only in clump B and derived an abundance of  $(7.9 \pm 1.7) \times 10^{-11}$  for the species. For comparison, Vasyunina et al. [65] detected  $\text{N}_2\text{H}^+(1-0)$  in all except one of their clumps (97.3% detection rate), and the scaled fractional abundances lie in the range of  $(0.15 - 7.74) \times 10^{-9}$ . Our derived  $\text{N}_2\text{H}^+$  abundance is roughly comparable to the lowest value in this range (a factor of  $1.9 \pm 0.4$  difference). Sanhueza et al. [44] reported a very high detection rate of 97% for the strongest hyperfine component of  $\text{N}_2\text{H}^+(1-0)$  (Table 4 therein), and the fractional abundances they derived are  $(0.1 - 9.2) \times 10^{-9}$ . The lowest value in this range agrees with the abundance of  $\text{N}_2\text{H}^+$  in clump B within a factor of  $1.3 \pm 0.3$ . The authors found that the  $\text{N}_2\text{H}^+$  abundance increases with clump evolution, and the low  $\text{N}_2\text{H}^+$  abundance found for the quiescent clump B is consistent with this evolutionary trend. The physics and chemistry behind this trend might be related to the release of  $\text{N}_2$  from dust grains as the temperature in the clump increases, after which it can react with  $\text{H}_3^+$  to form  $\text{N}_2\text{H}^+$ . This process is competing with the increasing abundance of CO, which is destroying  $\text{N}_2\text{H}^+$  in a process that produces  $\text{HCO}^+$  and  $\text{N}_2$ .

#### 4.4.5. $[\text{N}_2\text{H}^+]/[\text{HCO}^+]$ Abundance Ratio and $[\text{N}_2\text{D}^+]/[\text{N}_2\text{H}^+]$ Deuteration

Sanhueza et al. [44] found that the  $[\text{N}_2\text{H}^+]/[\text{HCO}^+]$  ratio can be used as a chemical clock, where the ratio decreases as the clump evolves from the intermediate stage (with enhanced 4.5  $\mu\text{m}$  emission or an embedded 24  $\mu\text{m}$  source) via an active stage (both enhanced 4.5  $\mu\text{m}$  emission and a 24  $\mu\text{m}$  source) to the red clump stage (association with bright 8  $\mu\text{m}$  emission). However, quiescent or IR-dark clumps were not found to follow this trend (see Figure 16 in their study). The  $[\text{N}_2\text{H}^+]/[\text{HCO}^+]$  abundance ratio for clump B is  $0.04 \pm 0.01$  (calculated from the column density ratio), which is two times lower than the median value of 0.08 derived by Sanhueza et al. [44] for their quiescent clumps, and also lower than the median value of 0.07 the authors derived for red clumps. Hence, our quiescent clump B also does not appear to follow the trend seen in the median values of  $[\text{N}_2\text{H}^+]/[\text{HCO}^+]$  by Sanhueza et al. [44].

Using a  $3\sigma$  intensity upper limit of  $T_{\text{MB}} < 4$  mK for  $\text{N}_2\text{D}^+(1-0)$  towards clump B, and assuming the same line width (FWHM) and  $T_{\text{ex}}$  as for the detected  $\text{N}_2\text{H}^+(1-0)$  line, we derived an  $\text{N}_2\text{D}^+$  column density upper limit of  $< 1.8 \times 10^{11} \text{ cm}^{-2}$ . This suggests that the  $[\text{N}_2\text{D}^+]/[\text{N}_2\text{H}^+]$  deuterium fractionation in clump B is  $< 0.05$ . For comparison, using observations with the IRAM 30 m telescope, Fontani et al. [68] derived  $[\text{N}_2\text{D}^+]/[\text{N}_2\text{H}^+]$  values in the range of  $\leq 0.004 - 0.02$  for their sample of ten high-mass young stellar objects. Fontani et al. [69] studied a sample of high-mass starless cores, high-mass protostellar objects (HMPOs), and ultracompact HII regions, and found  $[\text{N}_2\text{D}^+]/[\text{N}_2\text{H}^+]$  ratios of 0.012–0.7, 0.017– $\leq 0.4$ , and 0.017– $\leq 0.08$  for these different evolutionary stages. The average deuteration values were found to be  $\sim 0.26$ , 0.037, and 0.044, respectively, showing a decreasing trend in  $[\text{N}_2\text{D}^+]/[\text{N}_2\text{H}^+]$  when the source evolves from a starless stage to a HMPO. Gerner et al. [70] found that the  $[\text{N}_2\text{D}^+]/[\text{N}_2\text{H}^+]$  ratio in IRDCs drops from a median value of about 0.032 to about 0.009 in HMPOs (see Figure 5 therein). Based on observations with APEX, Lackington et al. [71] derived the  $[\text{N}_2\text{D}^+]/[\text{N}_2\text{H}^+]$  ratios between 0.002 and 0.23 for their sample of 29 cores in IRDCs. The  $[\text{N}_2\text{D}^+]/[\text{N}_2\text{H}^+]$  upper limit we derived for the 70  $\mu\text{m}$  dark clump B is consistent with many of the deuteration

levels observed in massive clumps and other IRDCs, but the present data do not allow us to quantify the potential effect that the environment might have on the deuteration in G1.75-0.08 (e.g., is it exceptionally low compared to the IRDCs in other parts of the Galaxy).

## 5. Conclusions

We used the Yebes 40 m and IRAM 30 m telescopes to make the first single-pointed spectral line observations towards the IRDC G1.75-0.08. These new observations were used to study the kinematics, dynamics, and molecular abundances of the cloud and its clumps. These new data allowed us to revise the gas velocity dispersion-dependent physical properties of the target source. Our main results are summarised as follows:

1. Three different molecular line transitions were unambiguously detected towards the clumps in G1.75-0.08 with Yebes, namely, HNC( $J_{K_a, K_c} = 4_{0,4} - 3_{0,3}$ ), HCN( $J = 1 - 0$ ), and HCO<sup>+</sup>( $J = 1 - 0$ ). With the IRAM 30 m telescope, we detected only N<sub>2</sub>H<sup>+</sup>( $J = 1 - 0$ ) towards clump B.
2. The HCN and HNC spectra exhibit two velocity components, which give an impression of red asymmetric line profiles that would be an indication of expanding gas motions.
3. Our new spectral line data support the view that the G1.75-0.08 filament is strongly subcritical (by a factor of  $11 \pm 6$ ), which is atypical compared to the general population of Galactic molecular cloud filaments.
4. Both clumps at the ends of the G1.75-0.08 filament were found to be gravitationally unbound ( $\alpha_{\text{vir}} > 2$ ). Because the clumps are 70  $\mu\text{m}$  dark and massive (several  $10^3 M_{\odot}$ ), they can be considered candidates for being high-mass starless clumps, but not prestellar.
5. The fractional abundances of the detected species in the target clumps are consistent with those observed in other IRDCs.

The IRDC G1.75-0.08 lies about 270 pc from the Galactic Centre in the CMZ, and could be an analogue of the CMZ cloud G0.253+0.016 (the Brick), which has been found to be a dynamically complex and hierarchically structured system rather than a single, coherent cloud [55]. High-resolution spectral line imaging of G1.75-0.08 would be needed to quantify the cloud's velocity structure; examine whether the orbital dynamics and shear motions in the CMZ could affect the cloud, as suggested in the case of the Brick; and test the hypothesis that the origin of the two clumps at the ends of the filament could be the result of gravitational focussing or the edge effect.

**Author Contributions:** Conceptualisation, O.M.; observations, O.M. and M.S.-G.; data reduction, O.M. and M.S.-G.; methodology, O.M. and M.S.-G.; formal analysis, O.M.; investigation, O.M. and M.S.-G.; data curation, O.M. and M.S.-G.; writing—original draft preparation, O.M.; writing—review and editing, O.M. and M.S.-G.; visualisation, O.M. All authors have read and agreed to the published version of the manuscript.

**Funding:** This research received no external funding.

**Institutional Review Board Statement:** Not applicable.

**Informed Consent Statement:** Not applicable.

**Data Availability Statement:** The Yebes and IRAM spectral line data that support the findings of this study are available upon request from the corresponding author. The APEX dust continuum data are openly accessible online through the ESO Science Archive (<https://archive.eso.org/wdb/wdb/eso/apex/form>).

**Acknowledgments:** We thank the two anonymous reviewers for providing useful comments and suggestions that helped to improve the quality of this paper. We are grateful to the staff at the Yebes 40 m telescope for performing the service mode observations for project 23A004 and to the staff at the IRAM 30 m telescope for performing the service mode observations presented in this paper. This research has made use of NASA's Astrophysics Data System Bibliographic Services, the NASA/IPAC

Infrared Science Archive, which is operated by the Jet Propulsion Laboratory, California Institute of Technology, under contract with the National Aeronautics and Space Administration, and *Astropy*<sup>8</sup>, a community-developed core Python package for Astronomy [72,73].

**Conflicts of Interest:** The authors declare no conflicts of interest.

## Abbreviations

The following abbreviations are used in this manuscript:

ALMA	Atacama Large Millimetre/submillimetre Array
APEX	Atacama Pathfinder EXperiment
ArTéMiS	Architectures de bolomètres pour des Télescopes à grand champ de vue dans le domaine sub-Millimétrique au Sol
CDMS	Cologne Database for Molecular Spectroscopy
CLASS	Continuum and Line Analysis Single-dish Software
CMZ	Central Molecular Zone
EMIR	Eight Mixer Receiver
FFTS	Fast-Fourier Transform Spectrometer
FWHM	Full width at half maximum
GILDAS	Grenoble Image and Line Data Analysis Software
HMPO	High-mass protostellar object
HPBW	Half-power beam width
IPAC	Infrared Processing & Analysis Center
IRAM	Institut de Radioastronomie Millimétrique
IRDC	Infrared dark cloud
JPL	Jet Propulsion Laboratory
LABOCA	Large APEX BOlometer CAmera
LSR	Local standard of rest
LTE	Local thermodynamic equilibrium
MALT90	Millimetre Astronomy Legacy Team 90 GHz
NASA	National Aeronautics and Space Administration
PWV	Precipitable water vapour
SFR	Star formation rate
VESPA	Versatile SPectrometer Array

## Notes

<sup>1</sup> [https://rt40m.oan.es/rt40m\\_en.php](https://rt40m.oan.es/rt40m_en.php) accessed on 1 February 2024.

<sup>2</sup> Grenoble Image and Line Data Analysis Software (GILDAS) is provided and actively developed by IRAM, and is available at [www.iram.fr/IRAMFR/GILDAS](http://www.iram.fr/IRAMFR/GILDAS) accessed on 28 December 2022.

<sup>3</sup> <https://splatalogue.online/> accessed on 1 February 2024.

<sup>4</sup> <https://cdms.astro.uni-koeln.de/> accessed on 1 February 2024.

<sup>5</sup> <http://spec.jpl.nasa.gov/> accessed on 1 February 2024.

<sup>6</sup> We note that for example in Miettinen [41], we used a column density formula, where the rotational degeneracy ( $g_J$ ) does not appear in the denominator, while in Equation (32) of Mangum & Shirley [40] it does (see also their Equation (33)). This difference arises from the different definitions of the dipole moment matrix element, which can be either  $|\mu_{ul}|^2 = \mu^2 S$ , where  $\mu$  is the permanent electric dipole moment and  $S$  is the line strength (Equation (62) in [40]), or  $|\mu_{ul}|^2 = \mu^2 S/g_J$  (see [42], where  $g_u = g_J$ ).

<sup>7</sup> Clump A and clump B were called SMM 15 and SMM 8 in the target field G1.87-014 of Miettinen [17] (see Figure 1 therein).

<sup>8</sup> [www.astropy.org](http://www.astropy.org) accessed on 1 April 2023.

## References

1. Péroul, M.; Omont, A.; Simon, G.; Seguin, P.; Ojha, D.; Blommaert, J.; Felli, M.; Gilmore, G.; Guglielmo, F.; Habing, H.; et al. First ISOCAM images of the Milky Way. *Astronomy and Astrophysics* **1996**, *315*, L165.
2. Egan, M.P.; Shipman, R.F.; Price, S.D.; Carey, S.J.; Clark F.O.; Cohen, M. A Population of Cold Cores in the Galactic Plane. *The Astrophysical Journal* **1998**, *494*, L199.
3. Peretto, N.; Fuller, G.A. The initial conditions of stellar protocluster formation. I. A catalogue of Spitzer dark clouds. *Astronomy and Astrophysics* **2009**, *505*, 405.

4. Jackson, J.M.; Finn, S.C.; Chambers, E.T.; Rathborne, J.M.; Simon, R. The "Nessie" Nebula: Cluster Formation in a Filamentary Infrared Dark Cloud. *The Astrophysical Journal Letters* **2010**, *719*, L185.
5. Kainulainen, J.; Ragan, S.E.; Henning, T.; Stutz, A. High-fidelity view of the structure and fragmentation of the high-mass, filamentary IRDC G11.11-0.12. *Astronomy & Astrophysics* **2013**, *557*, A120.
6. Henshaw, J.D.; Caselli, P.; Fontani, F.; Jiménez-Serra, I.; Tan, J. C.; Longmore, S. N.; Pineda, J. E.; Parker, R. J.; Barnes, A. T. Investigating the structure and fragmentation of a highly filamentary IRDC. *Monthly Notices of the Royal Astronomical Society* **2016**, *463*, 146.
7. Miettinen, O. The Seahorse Nebula: New views of the filamentary infrared dark cloud G304.74+01.32 from SABOCA, Herschel, and WISE. *Astronomy & Astrophysics* **2018**, *609*, A123.
8. Rathborne, J.M.; Jackson, J.M.; Simon, R. Infrared Dark Clouds: Precursors to Star Clusters. *The Astrophysical Journal* **2006**, *641*, 389.
9. Beuther, H.; Steinacker, J. The Protostar in the Massive Infrared Dark Cloud IRDC 18223-3. *The Astrophysical Journal* **2007**, *656*, L85.
10. Chambers, E.T.; Jackson, J.M.; Rathborne, J.M.; Simon, R. Star Formation Activity of Cores within Infrared Dark Clouds. *The Astrophysical Journal Supplement* **2009**, *181*, 360.
11. Battersby, C.; Bally, J.; Jackson, J.M.; Ginsburg, A.; Shirley, Y.L.; Schlingman, W.; Glenn, J. An Infrared Through Radio Study of the Properties and Evolution of IRDC Clumps. *The Astrophysical Journal* **2010**, *721*, 222.
12. Retes-Romero, R.; Mayya, Y.D.; Luna, A.; Carrasco, L. Infrared Dark Clouds and High-mass Star Formation Activity in Galactic Molecular Clouds. *The Astrophysical Journal* **2020**, *897*, 53.
13. Motte, F.; Bontemps, S.; Louvet, F. High-Mass Star and Massive Cluster Formation in the Milky Way. *Annual Review of Astronomy and Astrophysics* **2018**, *56*, 41.
14. Sanhueza, P.; Jackson, J.M.; Zhang, Q.; Guzmán, A. E.; Lu, X.; Stephens, I. W.; Wang, K.; Tatematsu, K. A Massive Prestellar Clump Hosting No High-mass Cores. *The Astrophysical Journal* **2017**, *841*, 97.
15. Siringo, G.; Kreysa, E.; Kovács, A.; Schuller, F.; Weiß, A.; Esch, W.; Gemünd, H.-P.; Jethava, N.; Lundershausen, G.; Colin, A. The Large APEX Bolometer CAmera LABOCA. *Astronomy and Astrophysics* **2009**, *497*, 945.
16. Miettinen, O. LABOCA 870  $\mu\text{m}$  dust continuum mapping of selected infrared-dark cloud regions in the Galactic plane. *Astronomy & Astrophysics* **2012**, *542*, A101.
17. Miettinen, O. A MALT90 study of the chemical properties of massive clumps and filaments of infrared dark clouds. *Astronomy & Astrophysics* **2014**, *562*, A3.
18. Foster, J.B.; Jackson, J.M.; Barnes, P.J.; Barris, E.; Brooks, K.; Cunningham, M.; Finn, S. C.; Fuller, G. A.; Longmore, S. N.; Mascoop, J. L.; et al. The Millimeter Astronomy Legacy Team 90 GHz (MALT90) Pilot Survey. *The Astrophysical Journal Supplement* **2011**, *197*, 25.
19. Foster, J.B.; Rathborne, J.M.; Sanhueza, P.; Claysmith, C.; Whitaker, J.S.; Jackson, J.M.; Mascoop, J.L.; Wienen, M.; Breen, S.L.; Herpin, F.; et al. Characterisation of the MALT90 Survey and the Mopra Telescope at 90 GHz. *Publications of the Astronomical Society of Australia* **2013**, *30*, e038.
20. Jackson, J.M.; Rathborne, J.M.; Foster, J.B.; Whitaker, J.S.; Sanhueza, P.; Claysmith, C.; Mascoop, J.L.; Wienen, M.; Breen, S.L.; Herpin, F.; et al. MALT90: The Millimetre Astronomy Legacy Team 90 GHz Survey. *Publications of the Astronomical Society of Australia* **2013**, *30*, e057.
21. Miettinen, O.; Mattern, M.; André, P. ArTéMiS imaging of the filamentary infrared dark clouds G1.75-0.08 and G11.36+0.80: Dust-based physical properties of the clouds and their clumps. *Astronomy & Astrophysics* **2022**, *667*, A90.
22. Révère, V.; André, P.; Le Pennec, J.; Talvard, M.; Agnès, P.; Arnaud, A.; Clerc, L.; de Breuck, C.; Cigna, J.-C.; Delisle, C.; et al. The ArTéMiS wide-field sub-millimeter camera: preliminary on-sky performance at 350 microns. *Proceedings of the SPIE* **2014**, *9153*, 915305.
23. André, P.; Révère, V.; Könyves, V.; Arzoumanian, D.; Tigé, J.; Gallais, P.; Roussel, H.; Le Pennec, J.; Rodriguez, L.; Doumayrou, E.; et al. Characterizing filaments in regions of high-mass star formation: High-resolution submillimeter imaging of the massive star-forming complex NGC 6334 with ArTéMiS. *Astronomy & Astrophysics* **2016**, *592*, A54.
24. Talvard, M.; Révère, V.; Le-Pennec, Y.; André, Ph.; Arnaud, A.; Clerc, L.; de Breuck, C.; Delisle, C.; Doumayrou, E.; Duband, L.; et al. Latest results and prospects of the ArTéMiS camera on APEX. *Proceedings of the SPIE* **2018**, *10708*, 1070838.
25. Petkova, M.A.; Kruijssen, J.M.D.; Kluge, A.L.; Glover, S.C.O.; Walker, D.L.; Longmore, S.N.; Henshaw, J.D.; Reissl, S.; Dale, J.E. The complex multiscale structure in simulated and observed emission maps of the proto-cluster cloud G0.253+0.016 ('the Brick'). *Monthly Notices of the Royal Astronomical Society* **2023**, *520*, 2245.
26. Henshaw, J.D.; Barnes, A.T.; Battersby, C.; Ginsburg, A.; Sormani, M.C.; Walker, D. L. Star Formation in the Central Molecular Zone of the Milky Way. In *Protostars and Planets VII*; Inutsuka, S., Aikawa, Y., Muto, T., Tomida, K., Tamura, M., Eds.; San Francisco: Astronomical Society of the Pacific; 2023; Volume 534, p. 83.
27. Tercero, F.; López-Pérez, J.A.; Gallego, J.D.; Beltrán, F.; García, O.; Patino-Esteban, M.; López-Fernández, I.; Gómez-Molina, G.; Diez, M.; García-Carreño; et al. Yebes 40 m radio telescope and the broad band Nanocosmos receivers at 7 mm and 3 mm for line surveys. *Astronomy & Astrophysics* **2021**, *645*, A37.
28. Silva, W.G.D.P.; Cernicharo, J.; Schlemmer, S.; Marcelino, N.; Loison, J.-C.; Agúndez, M.; Gupta, D.; Wakelam, V.; Thorwirth, S.; Cabezas, C.; et al. Discovery of  $\text{H}_2\text{CCCH}^+$  in TMC-1. *Astronomy & Astrophysics* **2023**, *676*, L1.

29. Agúndez, M.; Marcelino, N.; Tercero, B.; Jiménez-Serra, I.; Cernicharo, J. Abundance and excitation of molecular anions in interstellar clouds. *Astronomy & Astrophysics* **2023**, *677*, A106.
30. Tercero, B.; Marcelino, N.; Roueff, E.; Agúndez, M.; Cabezas, C.; Fuentetaja, R.; de Vicente, P.; Cernicharo, J. Doubly substituted isotopologues of HCCCN in TMC-1: Detection of D<sup>13</sup>CCCN, DC<sup>13</sup>CCN, DCC<sup>13</sup>CN, DCCC<sup>15</sup>N, H<sup>13</sup>C<sup>13</sup>CCN, H<sup>13</sup>CC<sup>13</sup>CN, HC<sup>13</sup>C<sup>13</sup>CN, HCC<sup>13</sup>C<sup>15</sup>N, and HC<sup>13</sup>CC<sup>15</sup>N. *Astronomy & Astrophysics* **2024**, *682*, L12.
31. Carter, M.; Lazareff, B.; Maier, D.; Chenu, J.-Y.; Fontana, A.-L.; Bortolotti, Y.; Boucher, C.; Navarrini, A.; Blanchet, S.; Greve, A.; et al. The EMIR multi-band mm-wave receiver for the IRAM 30-m telescope. *Astronomy & Astrophysics* **2012**, *538*, A89.
32. Pagani, L.; Daniel, F.; Dubernet, M.-L. On the frequency of N<sub>2</sub>H<sup>+</sup> and N<sub>2</sub>D<sup>+</sup>. *Astronomy and Astrophysics* **2009**, *494*, 719.
33. De Simone, M.; Fontani, F.; Codella, C.; Ceccarelli, C.; Lefloch, B.; Bachiller, R.; López-Sepulcre, A.; Caux, E.; Vastel, C.; Soldateschi, J. Deuterium and <sup>15</sup>N fractionation in N<sub>2</sub>H<sup>+</sup>. *Monthly Notices of the Royal Astronomical Society* **2018**, *476*, 1982.
34. Müller, H.S.P.; Schlöder, F.; Stutzki, J.; Winnewisser, G. The Cologne Database for Molecular Spectroscopy, CDMS: a useful tool for astronomers and spectroscopists. *Journal of Molecular Structure* **2005**, *742*, 215.
35. Pickett, H.M.; Poynter, R.L.; Cohen, E.A.; Delitsky, M.L.; Pearson, J.C.; Müller, H.S.P. Submillimeter, millimeter and microwave spectral line catalog *Journal of Quantitative Spectroscopy and Radiative Transfer* **1998**, *60*, 883.
36. Mangum, J. *Observing Modes Used in Radio Astronomy*; NRAO, 11 April 2006.
37. Pagani, L.; Frayer, D.; Pagani, B.; Lefèvre, C. Radio telescope total power mode: improving observation efficiency *Astronomy & Astrophysics* **2020**, *643*, A126.
38. Loughnane, R.M.; Redman, M.P.; Thompson, M.A.; Lo, N.; O'Dwyer, B.; Cunningham, M.R. Observations of HCN hyperfine line anomalies towards low- and high-mass star-forming cores. *Monthly Notices of the Royal Astronomical Society* **2012**, *420*, 1367.
39. Velilla, Prieto, L.; Sánchez, Contreras, C.; Cernicharo, J.; Agúndez, M.; Quintana-Lacaci, G.; Alcolea, J.; Bujarrabal, V.; Herpin, F.; Menten, K.M.; Wyrowski, F. New N-bearing species towards OH 231.8+4.2. HNCO, HNCS, HC<sub>3</sub>N, and NO. *Astronomy & Astrophysics* **2015**, *575*, A84.
40. Mangum, J.G.; Shirley, Y.L. How to Calculate Molecular Column Density. *Publications of the Astronomical Society of the Pacific* **2015**, *127*, 266.
41. Miettinen, O. What did the seahorse swallow? APEX 170 GHz observations of the chemical conditions in the Seahorse infrared dark cloud. *Astronomy & Astrophysics* **2020**, *639*, A65.
42. Turner, B.E. A Molecular Line Survey of Sagittarius B2 and Orion-KL from 70 to 115 GHz. II. Analysis of the Data. *Astrophysical Journal Supplement* **1991**, *76*, 617.
43. Fiege, J.D.; Pudritz, R.E. Helical fields and filamentary molecular clouds - I. *Monthly Notices of the Royal Astronomical Society* **2000**, *311*, 85.
44. Sanhueza, P.; Jackson, J.M.; Foster, J.B.; Garay, G.; Silva, A.; Finn, S.C. Chemistry in Infrared Dark Cloud Clumps: A Molecular Line Survey at 3 mm. *The Astrophysical Journal* **2012**, *756*, 60.
45. Miettinen, O. Dense cores in the Seahorse infrared dark cloud: physical properties from modified blackbody fits to the far-infrared-submillimetre spectral energy distributions. *Astronomy & Astrophysics* **2020**, *644*, A82.
46. Miettinen, O. A molecular line study of the filamentary infrared dark cloud G304.74+01.32. *Astronomy & Astrophysics* **2012**, *540*, A104.
47. Gregersen, E.M.; Evans, N.J.; Zhou, S.; Choi, M. New Protostellar Collapse Candidates: An HCO<sup>+</sup> Survey of the Class 0 Sources. *The Astrophysical Journal* **1997**, *484*, 256.
48. Gao, Y.; Lou, Y.-Q. Global collapses and expansions in star-forming clouds. *Monthly Notices of the Royal Astronomical Society* **2010**, *403*, 1919.
49. Kristensen, L.E.; van Dishoeck, E.F.; Bergin, E.A.; Visser, R.; Yıldız, U.A.; San Jose-Garcia, I.; Jørgensen, J.K.; Herczeg, G.J.; Johnstone, D.; Wampfler, S. F.; et al. Water in star-forming regions with Herschel (WISH). II. Evolution of 557 GHz 1<sub>10</sub>-1<sub>01</sub> emission in low-mass protostars. *Astronomy & Astrophysics* **2012**, *542*, A8.
50. Qin, S.-L.; Schilke, P.; Wu, J.; Liu, T.; Wu, Y.; Sánchez-Monge, Á.; Liu, Y. SMA observations of the W3(OH) complex: Dynamical differentiation between W3(H<sub>2</sub>O) and W3(OH). *Monthly Notices of the Royal Astronomical Society* **2016**, *456*, 2681.
51. Burkert, A.; Hartmann, L. Collapse and Fragmentation in Finite Sheets. *The Astrophysical Journal* **2004**, *616*, 288.
52. Heigl, S.; Hoemann, E.; Burkert, A. Taking off the edge - simultaneous filament and end core formation. *Monthly Notices of the Royal Astronomical Society* **2022**, *517*, 5272.
53. Hoemann, E.; Heigl, S.; Burkert, A. Filament collapse: a two phase process. *Monthly Notices of the Royal Astronomical Society* **2023**, *521*, 5152.
54. Hoemann, E.; Heigl, S.; Burkert, A. Filament fragmentation: density gradients suppress end-dominated collapse. *Monthly Notices of the Royal Astronomical Society* **2023**, *525*, 3998.
55. Henshaw, J.D.; Ginsburg, A.; Haworth, T.J.; Longmore, S.N.; Kruijssen, J.M.D.; Mills, E.A.C.; Sokolov, V.; Walker, D.L.; Barnes, A.T.; Contreras, Y.; et al. 'The Brick' is not a brick: a comprehensive study of the structure and dynamics of the central molecular zone cloud G0.253+0.016. *Monthly Notices of the Royal Astronomical Society* **2019**, *485*, 2457.
56. Mattern, M.; Kauffmann, J.; Csengeri, T.; Urquhart, J.S.; Leurini, S.; Wyrowski, F.; Giannetti, A.; Barnes, P.J.; Beuther, H.; Bronfman, L.; et al. SEDIGISM: the kinematics of ATLASGAL filaments. *Astronomy & Astrophysics* **2018**, *619*, A166.

57. Tress, R.G.; Sormani, M.C.; Girichidis, P.; Glover, S.C.O.; Klessen, R.S.; Smith, R.J.; Sobacchi, E.; Armillotta, L.; Barnes, A.T.; Battersby, C.; et al. Magnetic field morphology and evolution in the Central Molecular Zone and its effect on gas dynamics *Astronomy & Astrophysics* 2024, *submitted*, arXiv:2403.13048.
58. Baldeschi, A.; Elia, D.; Molinari, S.; Pezzuto, S.; Schisano, E.; Gatti, M.; Serra, A.; Merello, M.; Benedettini, M.; Di Giorgio, A.M.; et al. Distance biases in the estimation of the physical properties of Hi-GAL compact sources - I. Clump properties and the identification of high-mass star-forming candidates. *Monthly Notices of the Royal Astronomical Society* **2017**, *466*, 3682.
59. Traficante, A.; Fuller, G.A.; Billot, N.; Duarte-Cabral, A.; Merello, M.; Molinari, S.; Peretto, N.; Schisano, E. Massive 70  $\mu\text{m}$  quiet clumps I: evidence of embedded low /intermediate-mass star formation activity. *Monthly Notices of the Royal Astronomical Society* **2017**, *470*, 3882.
60. Sanhueza, P.; Contreras, Y.; Wu, B.; Jackson, J.M.; Guzmán, A.E.; Zhang, Q.; Li, S.; Lu, X.; Silva, A.; Izumi, N.; et al. The ALMA Survey of 70  $\mu\text{m}$  Dark High-mass Clumps in Early Stages (ASHES). I. Pilot Survey: Clump Fragmentation. *The Astrophysical Journal* **2019**, *886*, 102.
61. Li, S.; Sanhueza, P.; Zhang, Q.; Nakamura, F.; Lu, X.; Wang, J.; Liu, T.; Tatematsu, K.; Jackson, J.M.; Silva, A.; et al. The ALMA Survey of 70  $\mu\text{m}$  Dark High-mass Clumps in Early Stages (ASHES). II. Molecular Outflows in the Extreme Early Stages of Protocluster Formation. *The Astrophysical Journal* **2020**, *903*, 119.
62. Myers, P.C.; Hatchfield, H.P.; Battersby, C. Virial Clumps in Central Molecular Zone Clouds. *The Astrophysical Journal* **2022**, *929*, 34.
63. Chabrier, G.; Dumond, P. A Consistent Explanation for the Unusual Initial Mass Function and Star Formation Rate in the Central Molecular Zone (CMZ). *The Astrophysical Journal* **2024**, *966*, 48.
64. Li, S.; Sanhueza, P.; Zhang, Q.; Guido, G.; Sabatini, G.; Morii, K.; Lu, X.; Tafuya, D.; Nakamura, F.; Izumi, N.; et al. The ALMA Survey of 70  $\mu\text{m}$  Dark High-mass Clumps in Early Stages (ASHES). VIII. Dynamics of Embedded Dense Cores. *The Astrophysical Journal* **2023**, *949*, 109.
65. Vasyunina, T.; Linz, H.; Henning, T.; Zinchenko, I.; Beuther, H.; Voronkov, M. Chemistry in infrared dark clouds. *Astronomy & Astrophysics* **2011**, *527*, A88.
66. Rathborne, J.M.; Longmore, S.N.; Jackson, J.M.; Foster, J.B.; Contreras, Y.; Garay, G.; Testi, L.; Alves, J.F.; Bally, J.; Bastian, N.; et al. G0.253+0.016: A Centrally Condensed, High-mass Protocluster. *The Astrophysical Journal* **2014**, *786*, 140.
67. Rathborne, J.M.; Longmore, S.N.; Jackson, J.M.; Alves, J.F.; Bally, J.; Bastian, N.; Contreras, Y.; Foster, J.B.; Garay, G.; Kruijssen, J.M.D.; et al. A Cluster in the Making: ALMA Reveals the Initial Conditions for High-mass Cluster Formation. *The Astrophysical Journal* **2015**, *802*, 125.
68. Fontani, F.; Caselli, P.; Crapsi, A.; Cesaroni, R.; Molinari, S.; Testi, L.; Brand, J. Searching for massive pre-stellar cores through observations of  $\text{N}_2\text{H}^+$  and  $\text{N}_2\text{D}^+$ . *Astronomy and Astrophysics* **2006**, *460*, 709.
69. Fontani, F.; Palau, A.; Caselli, P.; Sánchez-Monge, Á.; Butler, M.J.; Tan, J.C.; Jiménez-Serra, I.; Busquet, G.; Leurini, S.; Audard, M. Deuteration as an evolutionary tracer in massive-star formation. *Astronomy & Astrophysics* **2011**, *529*, L7.
70. Gerner, T.; Shirley, Y.L.; Beuther, H.; Semenov, D.; Linz, H.; Albertsson, T.; Henning, Th. Chemical evolution in the early phases of massive star formation. II. Deuteration. *Astronomy & Astrophysics* **2015**, *579*, A80.
71. Lackington, M.; Fuller, G.A.; Pineda, J.E.; Garay, G.; Peretto, N.; Traficante, A. Deuteration in infrared dark clouds. *Monthly Notices of the Royal Astronomical Society* **2016**, *455*, 806.
72. Astropy Collaboration ; Robitaille, T.P.; Tollerud, E.J.; Greenfield, P.; Droettboom, M.; Bray, E.; Aldcroft, T.; Davis, M.; Ginsburg, A.; Price-Whelan, A.M.; et al. Astropy: A community Python package for astronomy. *Astronomy & Astrophysics* **2013**, *558*, A33.
73. Astropy Collaboration; Price-Whelan, A.M.; Sipőcz, B.M.; Günther, H.M.; Lim, P.L.; Crawford, S.M.; Conseil, S. ; Shupe, D.L.; Craig, M.W.; Dencheva, N.; et al. The Astropy Project: Building an Open-science Project and Status of the v2.0 Core Package. *The Astronomical Journal* **2018**, *156*, 123.

**Disclaimer/Publisher’s Note:** The statements, opinions and data contained in all publications are solely those of the individual author(s) and contributor(s) and not of MDPI and/or the editor(s). MDPI and/or the editor(s) disclaim responsibility for any injury to people or property resulting from any ideas, methods, instructions or products referred to in the content.